Indonesian Throughflow Partitioning between Leeuwin and South Equatorial Currents

LAURA K. GRUENBURG,[a] ARNOLD L. GORDON,[b] AND ANDREAS M. THURNHERR[b]

[a] *Stony Brook University, Stony Brook, New York*
[b] *Lamont-Doherty Earth Observatory, Columbia University, Palisades, New York*

(Manuscript received 7 October 2022, in final form 1 June 2023, accepted 3 June 2023)

ABSTRACT: Indonesian Throughflow (ITF) waters move along multiple pathways within the Indian Ocean. The western route is within the thermocline of the South Equatorial Current (SEC), and the southern route is via injection into the Leeuwin Current (LC) along western Australia. We use gridded Argo data to examine heat content anomaly (HCa) within three boxes in the eastern Indian Ocean, one adjacent to the ITF outflow from the Indonesian Seas (ITF box), the second in the eastern portion of the SEC (SEC box), and the third in the LC (LC box). Although interannual HCa variability in the SEC and ITF boxes is well correlated, a large increase in HCa within the ITF box does not appear in the SEC box in 2011 but is evident in the LC box. The 2011 change in the SEC–LC partitioning is investigated using GODAS reanalysis by examining the strength of the SEC and LC during a 2009 HCa increase within the ITF box and the subsequent increase in 2011. During 2009, a strong SEC and weakened LC spread the increased ITF HCa into the central Indian Ocean, whereas a weak SEC and strengthened LC during 2011 transmit the HCa signal to the south. Near-surface winds and mean sea level pressure from NCEP–NCAR reanalysis reveal that Ningaloo Niño events led to shifts in ocean circulation during 2000 and 2011. LC and SEC exports show a high negative correlation at interannual time scales, indicating that a reduction of outflow from one pathway is partially compensated by an increase from the other.

KEYWORDS: Indian Ocean; Heating; Interannual variability

1. Introduction

The Indonesian Throughflow (ITF) is a significant conduit for the transfer of Pacific Ocean water into the Indian Ocean, impacting the distribution of ocean heat within these two basins. The "global warming hiatus" of the 2000s was in part caused by a redistribution of heat from the tropical Pacific Ocean to the upper water column within the Indian Ocean (Nieves et al. 2015). Lee et al. (2015) showed that excess heat uptake by the Pacific Ocean was transferred via increased ITF to the Indian Ocean, creating a subsequent upper-ocean heat content increase. It was likewise concluded by Y. Zhang et al. (2018) that increasing advection from the ITF is the greatest contributor to an increase in upper-ocean heat content in the southern Indian Ocean during the last two decades. This increased advection of heat has had an effect on the Mascarene High region, weakening the atmospheric meridional pressure gradient over the Indian Ocean basin and influencing cross-equatorial winds (Vidya et al. 2020). Makassar Strait, which carries about 80% of the total ITF transport (Gordon et al. 2010), displays heat flux variability that is reflected in heat content variability in the eastern tropical Indian Ocean (Gruenburg and Gordon 2018).

While it is clear that the ITF plays an important role in interbasin heat exchange between the Indian and Pacific, the specific pathways of ITF spreading in the Indian Ocean can provide insight to where within the Indian the ITF water is distributed, with implications for local air–sea interaction and regional ecosystems. There are two identified avenues for the ITF to take: the South Equatorial Current (SEC) to the west between 10° and 15°S and the Leeuwin Current (LC) flowing southward along the western coast of Australia (Fig. 1).

The westward flowing SEC stretches from the Indo-Australian Basin to the eastern African margin (Wyrtki 1961; Schott and McCreary 2001), carrying ITF waters to the western part of the basin where the SEC splits and either joins the Agulhas Current via the Mozambique or East Madagascar Currents or flows to the north via the East African Coastal Current (Song et al. 2004). The SEC is driven by regional wind patterns and is also influenced by the ITF (Godfrey and Golding 1981). To the south, the LC is driven by the pressure gradient created by higher sea level off northwestern Australia, a result of the ITF (e.g., Thompson 1984; Godfrey and Ridgway 1985). The LC is strongest during austral winter when the prevailing northward winds weaken (e.g., Smith et al. 1991). Gordon et al. (1997) show the importance of the SEC pathway, identifying waters of up to 60% ITF origin transported by the SEC into the western Indian Ocean. Durgadoo et al. (2017) show that 6.1 Sv (1 Sv $\equiv 10^6$ m^3 s^{-1}) of Agulhas leakage has an ITF source, connected to the western Indian primarily via the SEC. van Sebille et al. (2014) use a model with Lagrangian particles to show that most of the ITF enters the SEC, though there is a smaller subset of these particles that are injected into the LC. Although these studies have shown that the ITF does flow through both the SEC and the LC, variability between these two routes is still poorly understood.

Supplemental information related to this paper is available at the Journals Online website: https://doi.org/10.1175/JPO-D-22-0205.s1.

Corresponding author: Laura K. Gruenburg, laura.gruenburg@stonybrook.edu

DOI: 10.1175/JPO-D-22-0205.1

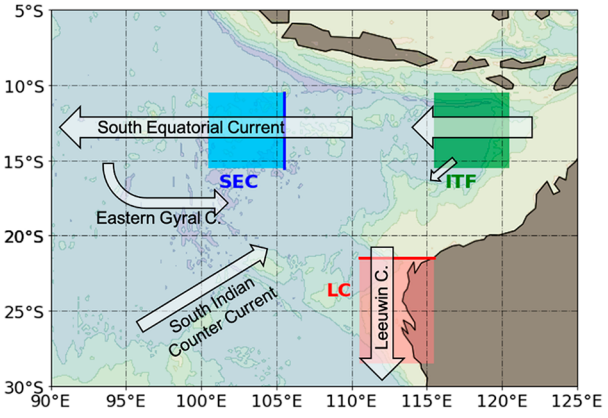

FIG. 1. The Indonesian Throughflow outflow area within the eastern tropical Indian Ocean. Currents are shown with black-outlined arrows. The three boxes where upper-ocean heat content was calculated are the ITF (green), SEC (blue), and LC (red). Velocities associated with the South Equatorial Current and the Leeuwin Current were examined across the thick blue and red lines, respectively.

Understanding how the ITF is partitioned between these two pathways is important for determining how and where the heat and freshwater from the Pacific spread across the Indian Ocean. As discussed above, increased westward SEC propagation, or westward propagation of eddies and Rossby waves from the Leeuwin region (Hirst and Godfrey 1993; Clarke and Li 2004; Waite et al. 2007), can bring ITF waters into the southern Indian Ocean, affecting upper-ocean heat content and cross-equatorial monsoonal winds. Increases in the SEC pathway can potentially impact the Agulhas Current and Leakage, although these effects would likely be seen at least a decade later. It is also possible that ITF waters in the Leeuwin only remain in the Indian Ocean briefly before making their way back toward the Pacific Ocean within the South Australia Current. This study uses Argo observations from 2005 to 2018 to track changes in upper-ocean heat content and GODAS reanalysis data to examine current velocity within the SEC and LC outflows of ITF water, with the aim of understanding the temporal variability of the partitioning between the two pathways.

2. Methods

Depth-integrated heat content of the water column was calculated in each of three boxes (Fig. 1) within the eastern tropical Indian Ocean (ETIO). The three boxes are the ITF box (10.5°–15.5°S and 115.5°–120.5°E), the SEC box (10.5°–15.5°S and 100.5°–105.5°E), and the LC box (21.5°–28.5°S and 110.5°–115.5°E). The SEC and ITF boxes are located within the ITF low-salinity buoyant plume designated by Andersson and Stigebrandt (2005) (AS box; 10°–15°S at 100°–120°E). The ITF box is positioned at the far eastern end of the AS box and encompasses the waters leaving the Indonesian Seas through the Timor and Ombai Passages, together making up roughly 80% of the total outflow [based on International Nusantara Stratification and Transport (INSTANT) program values; Gordon et al. 2010]. The SEC box is in the far western portion of the AS box and encompasses the ITF outflow that will enter the Indian Ocean within the SEC. The half degree offset between the AS box bounds and those of the SEC and ITF boxes is related to the 1° × 1° spatial resolution of the gridded Argo dataset that provides variables on the half degree. The LC box is located south of the AS box along the west Australian coast.

The upper-ocean heat content (HC; above 25.5σ) in each box was calculated using the following equation:

$$Q_{25.5} = \int_{25.5}^{\text{surface}} \theta \rho c_p \, dz. \tag{1}$$

The parameters θ (potential temperature) and ρ (density) were acquired from gridded Argo datasets (http://apdrc.soest.hawaii.edu/projects/argo/.). The Argo datasets have 1° × 1° spatial resolution with monthly temporal resolution from 2005 through 2018. Heat content was calculated above an isopycnal instead of a fixed depth to account for changes in heat content induced by thermocline heaving. We compare heat content anomaly (HCa; calculation of anomaly described below) calculated above a fixed depth of 300 m with that above 25.5σ in Fig. 2. Although the magnitude of the HCa from the two methods is different, primarily because of different volumes used in the integration, the heat content variability is quite similar in both cases across all three boxes. We use HCa above the 25.5σ surface in all further analysis.

As the ITF waters tend to spread within the Indian Ocean thermocline (Gordon 1986; Gordon et al. 1997), we chose to investigate HCa above the 25.5σ surface as it is within the climatological midthermocline, near 200 m, for all three boxes (Fig. S1 in the online supplemental material). At each grid point within the three boxes at monthly time steps, the θ and

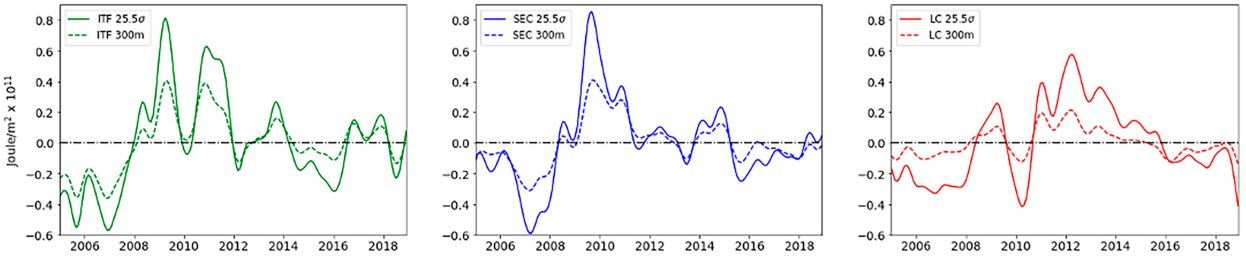

FIG. 2. Heat content anomaly per square meter above 300 m (dashed lines) and heat content anomaly per square meter above 25.5σ (solid lines) within the (left) ITF, (center) SEC, and (right) LC boxes from Fig. 1 (green, blue, and red, respectively).

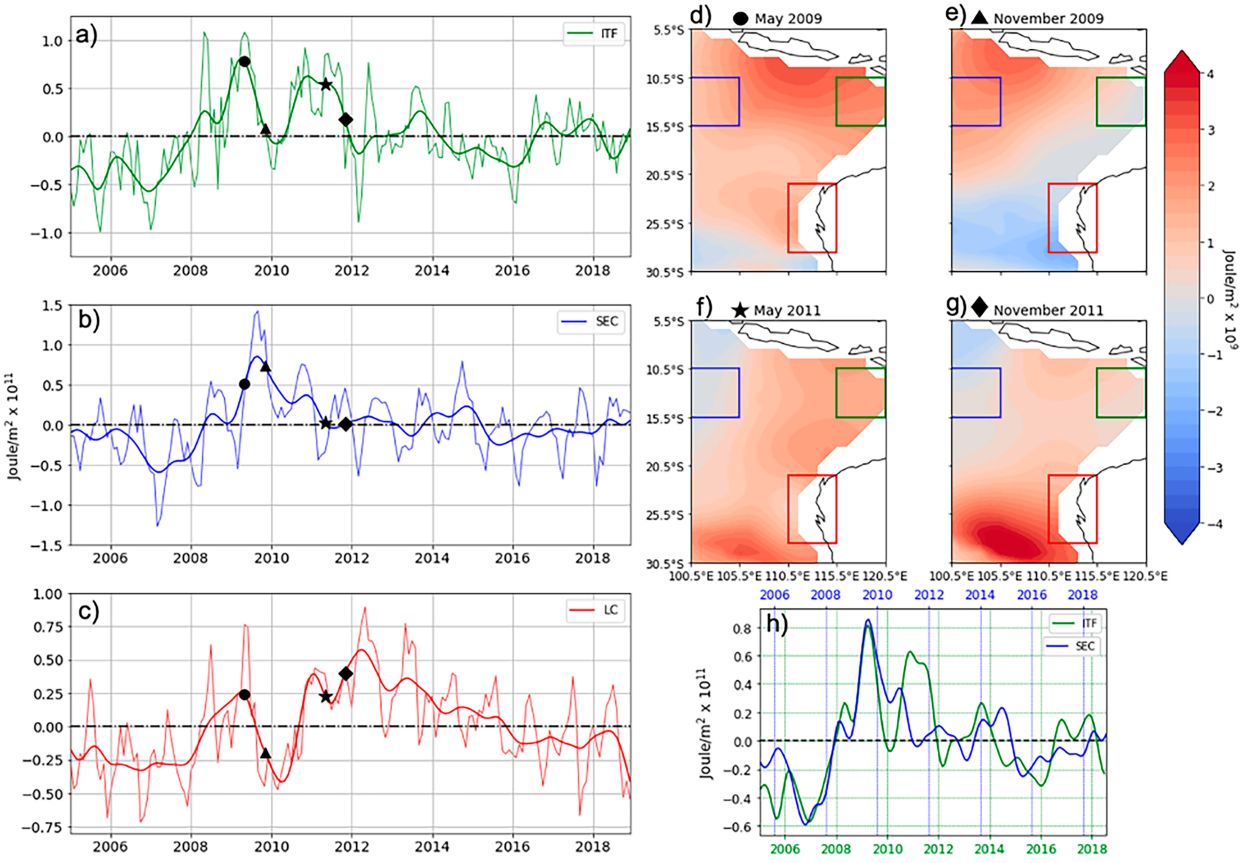

FIG. 3. Heat content anomaly per square meter above the 25.5σ surface in each of (a) ITF, (b) SEC, and (c) LC boxes from Fig. 1, with the thin line showing monthly anomaly from the time average mean, the thick line showing results with the seasonal cycle removed by subtraction of climatological monthly means; a Butterworth low-pass filter removed high-frequency variability. The black circle, triangle, star, and diamond correspond to the contour plots in (d)–(g), which show HCa per square meter above the 25.5σ surface at each 1° × 1° grid point in the Argo dataset (reds indicate positive heat content anomaly, and blues indicate negative heat content anomaly); shown are (d) May and (e) November of 2009 (a positive heat content anomaly is seen propagating from the ITF box westward toward the SEC box) and (f) May and (g) November of 2011 (during this time period, heat content anomaly is advected southward from the ITF box into the LC region) Also shown is (h) HCa per square meter above the 25.5σ surface in ITF (green) and SEC (blue) boxes. The SEC box (top blue x axis) is shown lagged 5 months behind the ITF box (lower green x axis). At this lag the two are well correlated with $r = 0.7$. The second large positive HCa in the ITF box during 2010/11 is not reflected later in the SEC box.

potential density σ variables were linearly interpolated from standard depths (fine resolution close to the surface with increased spacing at depth) to 10-m intervals from the surface to the 25.5σ surface. Heat content per square meter was then calculated using Eq. (1) with $c_p = 4000$ J kg^{-1} K^{-1}. HC values for each grid point within the box were then summed. Heat content per square meter is used instead of total heat content over the area of the box because of the different sizes of the boxes. As a result of shallow topography, not all grid points within the Leeuwin and ITF boxes contained data. To verify that Argo floats were present in the boxes, the number of profiles per year was calculated and is shown in Fig. S2 in the online supplemental material. HCa was calculated by removing the climatological monthly mean HC values at each grid point at each monthly time step. To remove high-frequency variability (higher than once per year), a Butterworth low-pass filter was applied to the resulting time series.

The HCa within the ITF box was compared with those in the other two boxes. First the 12-month running mean of the SEC box HCa was cross correlated at monthly lags (1-month time step for 2 years) with the ITF box. Correlations were considered significant if p values were less than 0.05.

Next, we examined the changes in the zonal velocity (SEC) and meridional velocity (LC) within the upper water column. The SEC section (blue line in Fig. 1) is the most eastward boundary of the box (105°E from 15° to 10°S). The Leeuwin section (red line in Fig. 1) cuts across the northern boundary of the LC box, at 21°S from 110° to 115°E. The southward velocities across the LC section and westward velocities across the SEC section were investigated using meridional and zonal velocities in the upper 400 m from GODAS reanalysis (Behringer and Xue 2004). GODAS is a gridded global dataset at a spatial resolution of $\frac{1}{3}$° latitude by 1° longitude of monthly mean variables. Zonal and meridional components

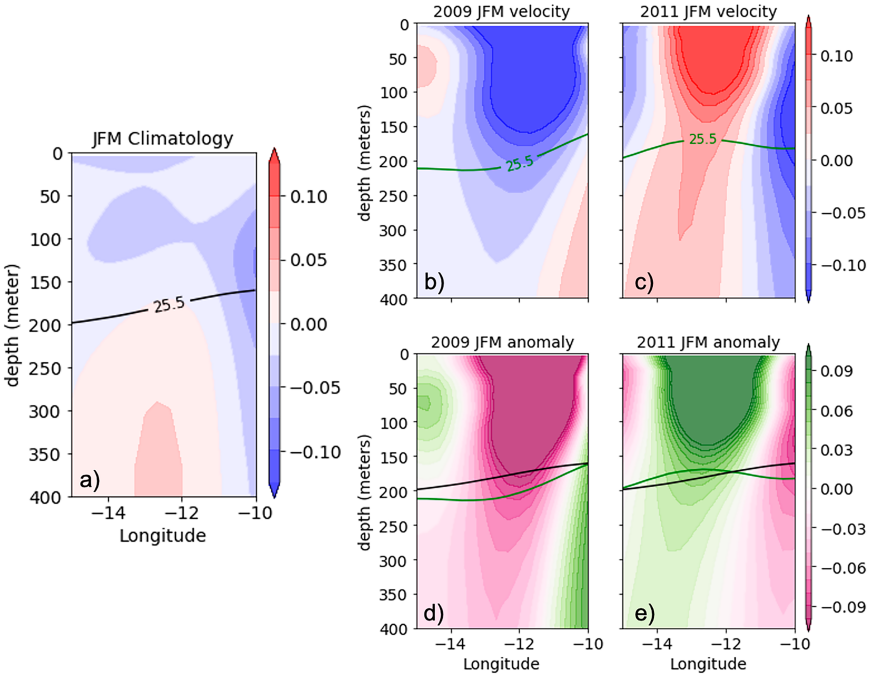

FIG. 4. Zonal velocity across 105°E, the easternmost boundary of the SEC box: (a) Climatological velocity of averaged January–March (JFM), with blue as westward and red as eastward velocities (m s^{-1}). The 25.5σ isopycnal is shown as a black line. JFM averaged velocity for (b) 2009 and (c) 2011, with red and blue shading as in (a). The 25.5σ isopycnal is shown in green. JFM anomaly from the climatology for (d) 2009 and (e) 2011. Purples indicate anomalous westward velocity, and greens indicate anomalous eastward velocity (m s^{-1}). Climatological and JFM averaged 25.5σ isopycnals are shown in black and green, respectively. A strong westward flow is present in 2009, whereas 2011 shows an eastward flow.

of current velocity were retrieved at 28 depth levels (5, 15, 25, 35, 45, 55, 65, 75, 85, 95, 105, 115, 125, 135, 145, 155, 165, 175, 185, 195, 205, 215, 225, 238, 262, 303, 366, and 459 m) from 1980 through 2019. When examining the anomaly, we subtracted the climatological monthly mean values. These climatological values were created by averaging from 2005 through 2018 for consistency with the Argo data.

Next, we aimed to quantify the transport out of the Indo-Australian basin by the SEC and LC pathways. Volume transport across the SEC section (blue line in Fig. 1) was calculated at the eastern boundary of SEC box (105°E from 15° to 10°S). Transport across the Leeuwin (LC) section cuts across the northern boundary of the LC box (21.5°S from 110° to 115°E). The southward transport along the LC section and westward transport across the SEC section were investigated using meridional and zonal velocities averaged above the 25.5σ isopycnal using the GODAS reanalysis described above. Monthly mean anomaly from the climatology is calculated the same way as with HCa.

To further understand the relationship between the two outflow pathways, a lag correlation between the two was performed. To investigate which external forcings play a role in transport variability, the two time series were compared with the Niño-3.4 index and dipole mode index (DMI), as well as to the zonal and meridional components of near-surface wind velocity, along with sea surface height anomaly. NCEP–NCAR Reanalysis 1 (Kalnay et al. 1996) zonal and meridional components of wind speed at 1000 hPa are at 2.5° × 2.5° spatial resolution monthly from January 1949 through December 2018. Wind stress curl was approximated using

$$\tau_{x,y} = \rho C_D U_{x,y} \mathbf{U}_{x,y} \quad \text{and} \tag{2a}$$

$$\text{curl}\tau = \frac{\partial \tau_x}{\partial y} - \frac{\partial \tau_y}{\partial x}. \tag{2b}$$

where $\tau_{x,y}$ is the wind stress in the zonal (x) or meridional (y) direction; ρ is air density, approximated as 1.22 kg m^{-3}; C_D is the drag coefficient, given as 0.0013; and $U_{x,y}$ are the zonal and meridional components of wind speed. Sea surface height anomaly from the geoid (SSHg) was included in the GODAS reanalysis dataset. The SEC and LC transport time series were compared with the winds in a box bounded by 50°S to 22.5°N and 50° to 150°E, encompassing the majority of the Indian Ocean and a portion of the Pacific Ocean containing the western Pacific warm pool. At each grid point within this domain the zonal, and meridional monthly wind speed anomalies, and monthly wind stress curl anomalies were cross correlated with the SEC and LC transport anomalies at monthly lags for 2 years. The same procedure was performed using SSHg monthly anomalies within the box bounded by

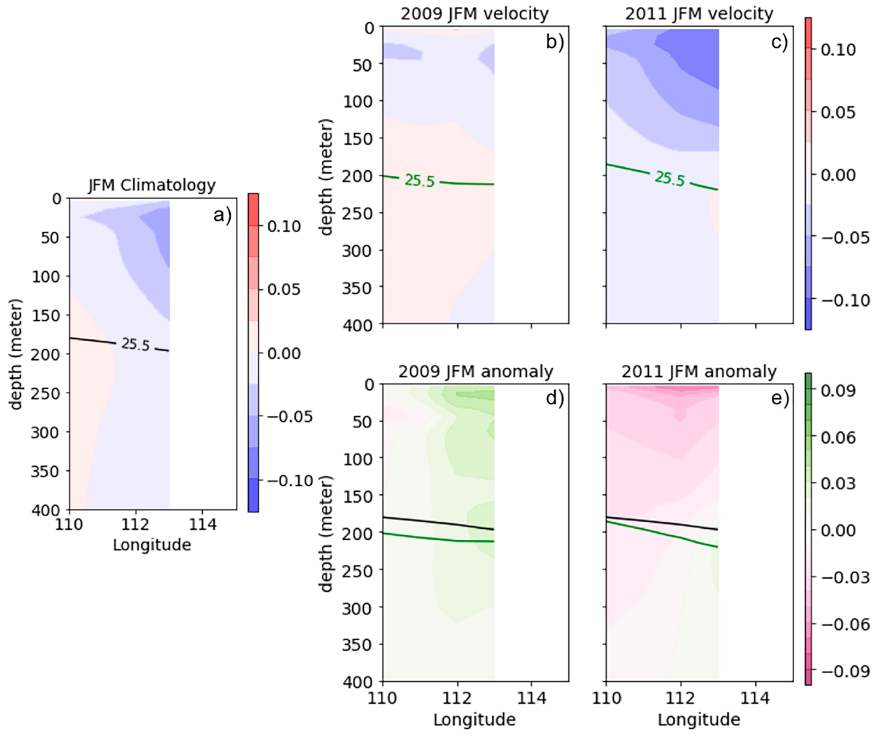

FIG. 5. Similar to Fig. 4, but for meridional velocity across 21.5°S, the top of the LC box. In (a), blue indicates southward velocities and red is northward velocities (m s^{-1}). In (d) and (e), purples indicate a strengthened southward velocity and greens indicate a weakened southward velocity. A weakening of southward flow is seen in 2009, whereas 2011 shows a strong increase in southward flow.

41.17°–1.17°S and 40.5°–129.5°E encompassing the southern Indian Ocean.

3. Results

a. Heat content

Time series of HCa per square meter are plotted in Figs. 3a–c. The mean HCs calculated using original monthly mean data are $6.4 \times 10^{11} \pm 4.3 \times 10^{10}$ in the ITF box, $6.3 \times 10^{11} \pm 4.3 \times 10^{10}$ J m^{-2} in the SEC box, and $2.7 \times 10^{11} \pm 3.4 \times 10^{10}$ J m^{-2} in the LC box. A strong seasonal cycle is present in both the SEC and LC boxes. The SEC experiences maximum HCa per meter squared in September–October and minimum HCa per meter squared in March–April. Maximum HCa per meter squared in the LC box occurs in April–June, with a minimum in September–November. The SEC box is best correlated with the ITF box ($r = 0.7$) when the SEC box lags the ITF box by 5 months. The first positive HCa peak in the ITF time series during 2009 is present 5 months later in the SEC box; however, the second ITF HCa peak in 2011 does not appear in the SEC box but does appear in the LC box (Figs. 3d–h).

b. Velocity across sections

We next examine the velocity across the SEC and LC sections (Fig. 1) during 2009 (first peak in ITF HCa) and 2011 (second peak). During early 2009 there was an increase in westward velocity in the SEC predominately in the upper 200 m during January–March (JFM) with maximum anomalies around −0.32 m s^{-1} within the surface layer (Fig. 4). Conversely, during 2011 we see a strong negative anomaly, with an anomalous eastward flow with maximum values of 0.26 m s^{-1}, within the upper 200 m of the SEC during JFM. In the LC region, 2009 is marked by slightly weaker southward flow in the upper water column than climatological values (Fig. 5). During 2011 an increase in southward flow is present.

c. Near-surface winds and mean sea level pressure

The zonal and meridional components of wind and the mean sea level pressure (MSLP) reveal strong anomalies in 2011 (Figs. 6 and 7). In JFM of that year there were strong positive (eastward) zonal wind anomalies along 10°S from 80° to 110°E. Meridional winds show negative anomalies (weaker northward) along the western coast of Australia as well as in the Indo-Australian Basin during JFM. MSLP reveals a region of low pressure located over northwest Australia, and the MSLP anomaly further indicates that anomalously low MSLP extended off the west Australian Coast. These pressure anomalies are consistent with a cyclonic circulation that produced the zonal and meridional wind anomalies seen in 2011. When 2009 is examined, we see no consistent and well defined positive or negative anomalies in zonal winds. There is a small positive meridional wind (more northward) anomaly over our

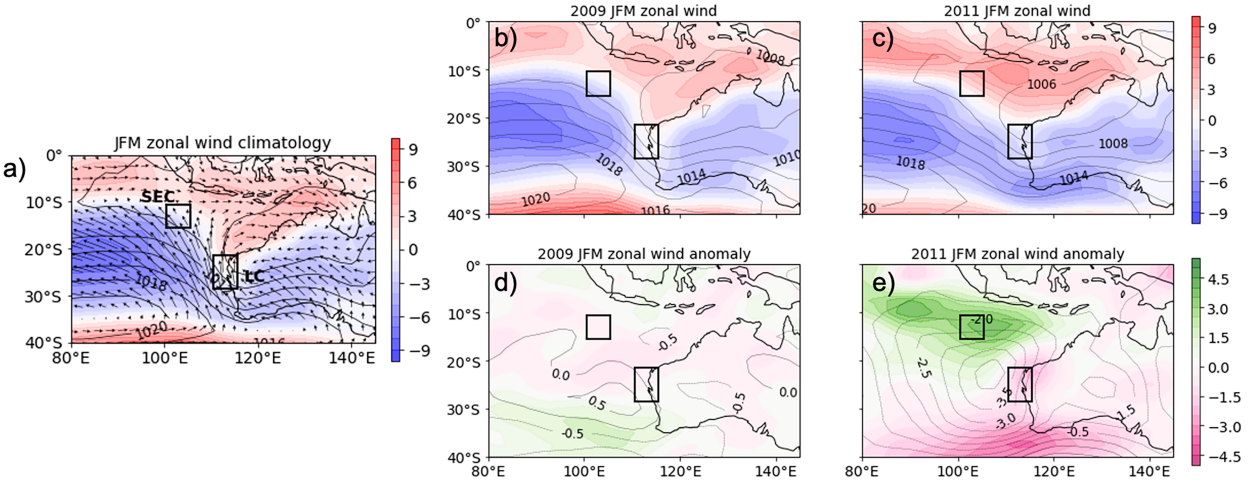

FIG. 6. Zonal wind speed (m s^{-1}) at 1000 hPa (colored shading) and MSLP (hPa; black contour lines): (a) Climatological average of JFM, with reds indicating westerly winds and blues indicating easterly winds. Vectors show wind velocity. Zonal winds and MSLP during JFM of (b) 2009 and (c) 2011, with colored shading as in (a). Also shown for (d) 2009 and (e) 2011 are JFM zonal wind anomaly from the climatology (colored shading, with greens as positive anomalies that are stronger eastward and weaker westward and purples as negative anomalies that are stronger westward and weaker eastward) and MSLP anomalies (black contours). During 2011, an anomalous low pressure center is present off the west Australian coast, with positive zonal wind anomalies present along 10°S.

LC box for the first three months of 2009. MSLP reveals only a small positive pressure anomaly along the west Australian Coast during the same time.

d. *Transport across sections*

The mean transport across the SEC section was −7.0 ± 5.5 Sv (negative transport indicates westward flow, *out* of ETIO region), and the mean transport across the LC section was −1.7 ± 1.7 Sv, with the stated uncertainties indicating 1 standard deviation. The large standard deviation is indicative of a strong seasonal cycle. When we compare the LC and SEC time series, we see that the monthly means are well correlated ($r = -0.63$). When examining the anomaly, the two time series are poorly correlated (overall $r = -0.36$; Figs. 8 and 9). It is noted that Fig. 9 shows three distinct clusters in time of transport data. We examine these three groups individually (A: 2006–11, B: 2012–15, and C: 2016–18) and see that LC and SEC are highly anticorrelated with $r = -0.8$, -0.6, and -0.8 for groups A, B, and C, respectively. Although when broken into smaller groups these time series contain fewer data points on which to perform the correlation, the p values for all three correlation coefficients are well below 0.05. LC transport anomaly is well

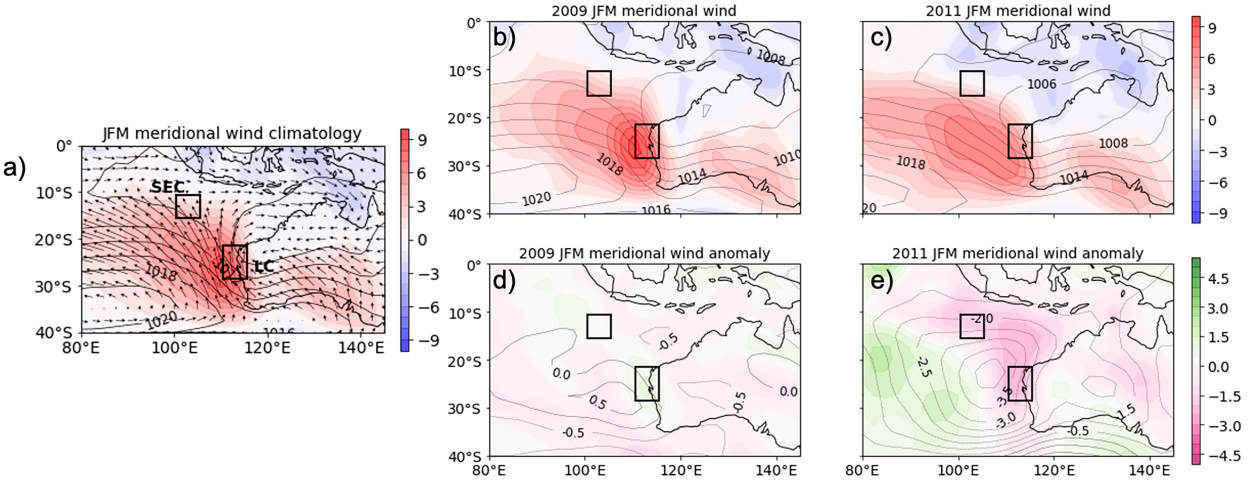

FIG. 7. As in Fig. 6, but for meridional wind speed. In (a), reds indicate southerly winds and blues indicate northerly winds. In (d) and (e), the positive anomalies are stronger northward and weaker southward and the negative anomalies are stronger southward and weaker northward. The low pressure center off the west Australian coast during 2011 is associated with anomalous cyclonic atmospheric circulation and a weakening of southerly winds in the Leeuwin Current region. Conversely, during 2009 MSLP anomalies are weakly positive west of Australia and meridional wind anomalies are weakly positive over the Leeuwin Current region.

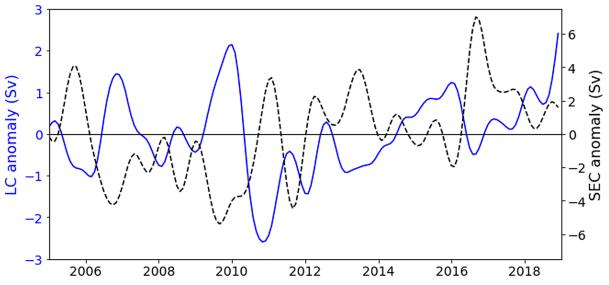

FIG. 8. LC and SEC transport anomalies above the 25.5σ surface during the Argo observational time period. LC is shown as the blue line, and the SEC transport is shown as the dashed black line. The maximum in southward LC transport anomaly in 2011 can be seen with an accompanying peak in eastward SEC transport anomaly.

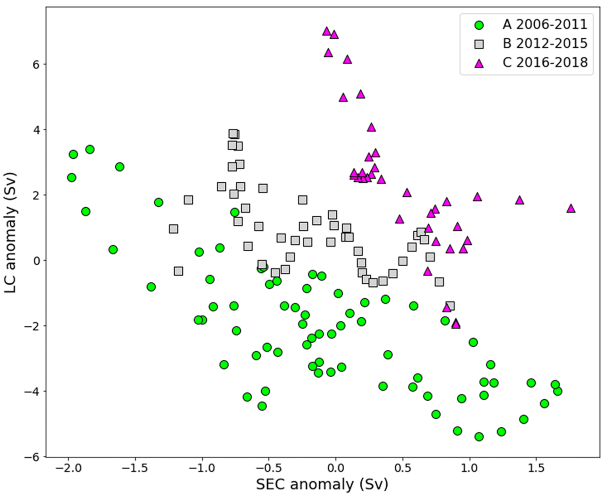

FIG. 9. Scatterplot depicting SEC transport anomaly on the x axis and LC transport anomaly on the y axis. Although the overall correlation between the transports in the two currents is low ($r = -0.36$), visually the data cluster into three different time periods that are all associated with high but different anticorrelations between the SEC and LC transport anomalies: period A (2006–11; $r = -0.8$), period B (2012–15; $r = -0.6$), and period C (2016–18; $r = -0.7$).

correlated ($r = 0.74$) with the Niño-3.4 index whereas the SEC transport anomaly is not well correlated with Niño-3.4 ($r = -0.22$). The SEC and LC transport anomalies are significantly, although not highly, correlated with DMI ($r = -0.31$ and 0.37 for the SEC and LC, respectively).

When compared with the zonal and meridional components of the wind velocity, the SEC transport anomaly shows highest correlation ($|r| > 0.5$; Fig. S3 in the online supplemental material) with zonal wind anomaly over the tropical Indian Ocean and with meridional wind anomaly off the western coasts of Sumatra and Java (Fig. S3). The SEC transport anomaly is also well correlated with the wind stress curl anomaly in the tropical Indian Ocean. The LC transport anomaly shows the highest negative correlation ($r < -0.5$) with zonal wind anomaly over the Flores Sea and the highest positive correlation ($r > 0.5$) with zonal wind anomaly off the northwest coast of Australia. The highest correlation between LC and meridional wind anomaly occurs off the northwest coast of Australia and to the south of Sumatra ($r > 0.5$).

The SEC shows a high correlation ($r < -0.7$) with SSHg in the region immediately to the west of the section. The LC shows the highest correlation ($r < -0.7$) along the west and north Australian coasts (Fig. S4 in the online supplemental material) with higher SSHg in this region associated with an increase in southward LC flow. SSHg along the west Australian coast has been linked to both local and remote (tropical Pacific) wind stress variability (Kusunoki et al. 2021).

4. Discussion

Our results clearly indicate a change in circulation during 2011 within the eastern tropical Indian Ocean when compared with 2009. The year 2011 is of particular importance in the region because it was a very strong Ningaloo Niño. A Ningaloo Niño is defined by anomalously high SST within the region of 32°–26°S, 112°–115°E [Ningaloo Niño index (NNI); Marshall et al. 2015; Fig. 10], and during 2011 this region experienced over 1°C of surface warming (Feng et al. 2013).

Our analysis of wind speed and MSLP is consistent with that of Feng et al. (2013), who examined this 2011 Ningaloo Niño event in detail and concluded that the weakened southerly winds off the west Australian Coast had a large impact on the increasing LC flow. We find that in addition to the anomalous behavior of the LC, this period is also characterized by the reversal of flow across the SEC section (Fig. 4). Our results indicate that this reversal of the SEC during 2011 was also an important factor in the warming within the LC region, as decreased transport through the SEC pathway led to an increase in SSHg in the Indo Australian basin, thus increasing the north–south pressure gradient along the LC pathway. During this time a reduction in westward SEC transport decreased the efficient export of heat from Indonesian Seas westward out of the Indo-Australian, instead the strengthened LC carried these warm ITF waters to the south. Benthuysen et al. (2014) agree with this conclusion and find that $^2/_3$ of the anomalous warming in the LC region during this time period was due to advection as opposed to changes in air–sea interaction. Our results from 2009 indicate an opposing circulation to that of 2011, with a strong SEC during the early part of the year that transported heat into the central Indian Ocean, and a

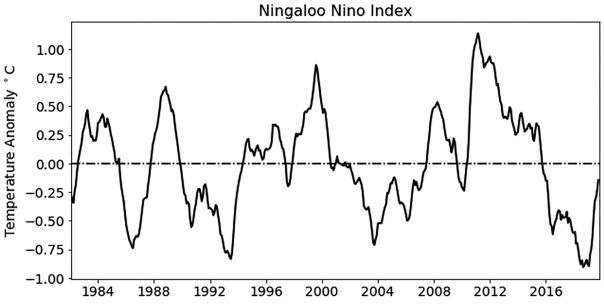

FIG. 10. Ningaloo Niño index as defined by the sea surface temperature anomaly within the region 32°–26°S, 112°–115°E.

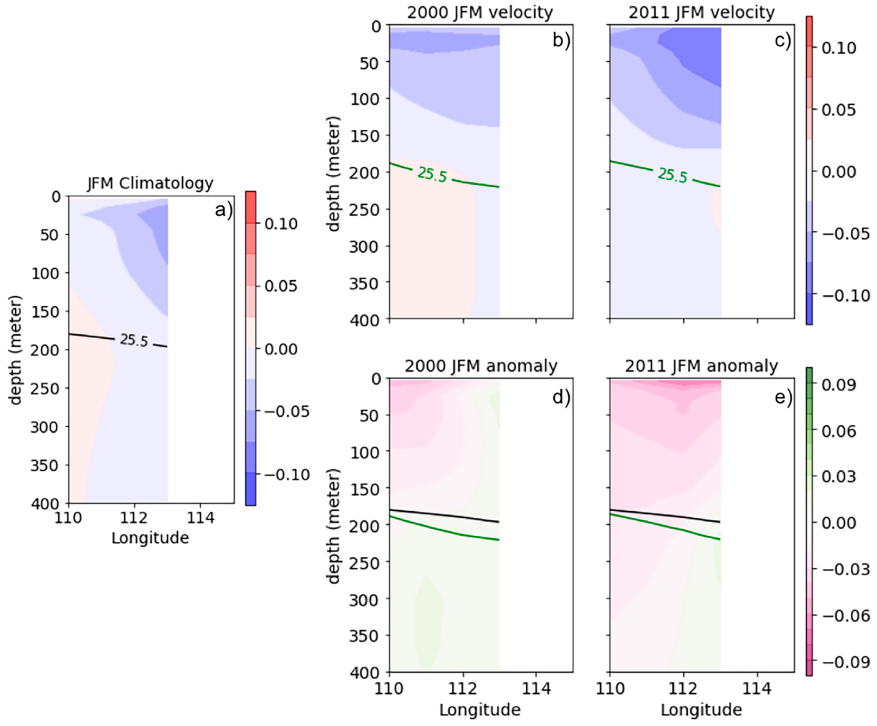

FIG. 11. Meridional velocity (m s^{-1}) across 21.5°S, the top of the LC box: (a) The JFM climatology, with blues indicating southward velocity and reds indicating northward velocity. The 25.5σ isopycnal is shown by the black line. JFM meridional velocity during (b) 2000 and (c) 2011, with colors as in (a). The 25.5σ isopycnal is shown by the green line. The (d) 2000 and (e) 2011 anomaly from the climatology, with purples as negative anomalies (stronger southward flow) and greens as positive anomalies (stronger northward flow and weaker southward flow). The climatological and 2000/2011 25.5σ isopycnals are shown by the black and green lines, respectively. Both 2000 and 2011 experience an increase in southward Leeuwin Current velocities during JFM.

weakened LC. Wind anomalies during 2009 were relatively weak, and the NNI was close to zero indicating neutral conditions. Although the Argo dataset is too short to have recorded another strong Ningaloo Niño event, we use the GODAS reanalysis to examine the SEC and LC velocities and regional MSLP, as well as NCEP–NCAR reanalysis for wind speed, from another smaller Ningaloo Niño event during 2000 (Figs. 11–14). Although the anomalies are smaller, they are similar to those of 2011, with a reversal of flow within the SEC region, an increase in LC transport, and a small low pressure anomaly off the northwestern coast of Australia driving a cyclonic circulation. Our results show the importance of the characteristic Ningaloo Niño atmospheric low and anomalous cyclonic circulation (Kataoka et al. 2014) to the upper-ocean export pathways of the ITF.

The strong correlation between ENSO and the LC transport is consistent with other studies (e.g., Feng et al. 2003). Meyers (1996) examine XBT line IX1 that connects western Australia with the western tip of Java and found that an ENSO signal was easily apparent in SST, dynamic height, and thermocline depth in the LC region, but that this signal was not as pronounced in the northern portion of the section (SEC region). This is consistent with our finding that SEC outflow is not well correlated with Niño-3.4. It should be noted that Ningaloo Niño events discussed above are often associated with La Niña conditions in the Pacific, although this is not always the case as they may develop independently due to local air–sea feedbacks (e.g., Tozuka et al. 2014; Marshall et al. 2015; L. Zhang et al. 2018; Kataoka et al. 2018). The results of the correlation with DMI are less straightforward. The long lag time (>1.5 years for both time series) is difficult to explain, especially with regard to the SEC section, which is partially in the eastern box used to calculate the index. The correlations between the DMI and these transport time series likely do not indicate a direct cause and effect relationship between changing DMI and transport. It is more likely that these correlations simply reflect the interconnected nature of the DMI and other regional climate forcing such as ENSO.

The correlation between the SEC and LC transport monthly mean time series reflects an alignment of seasonal cycles, as the SEC displays a minimum transport during April–May and a maximum outflow during September–October whereas the LC shows a minimum transport September/October and a maximum transport in April–May. There is a slight offset with the LC showing a maximum on average during April and the SEC showing a minimum on average during May, so the seasonal cycles are not identically opposite. The high negative correlations of the three clusters of LC and SEC anomalies

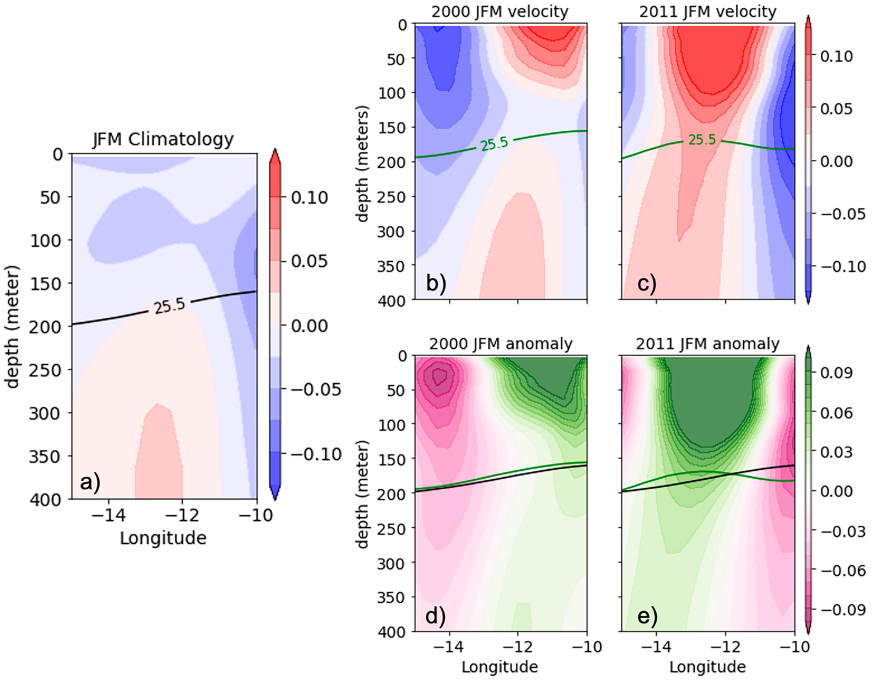

FIG. 12. Similar to Fig. 11, but for zonal velocity across 105°E, the easternmost boundary of the SEC box. In (a), blues indicate westward velocity and red indicates eastward velocity. In (d) and (e), purples indicate stronger westward flow and weaker eastward flow and greens indicate stronger eastward flow and weaker westward flow. An increase of westward flow is present during JFM of both 2000 and 2011, although the increase was stronger in 2011.

indicate that when one pathway's export is reduced, there is some compensation by the other. This is not a perfect balance, though, because the LC transport is much smaller than the SEC transport. The clustering present in Fig. 9 reflects a weakening in the SEC over time as well as a trend toward a smaller amplitude seasonal cycle in both the LC and the SEC. As mentioned above, the LC is well correlated with ENSO and this trend toward a weaker seasonal cycle could

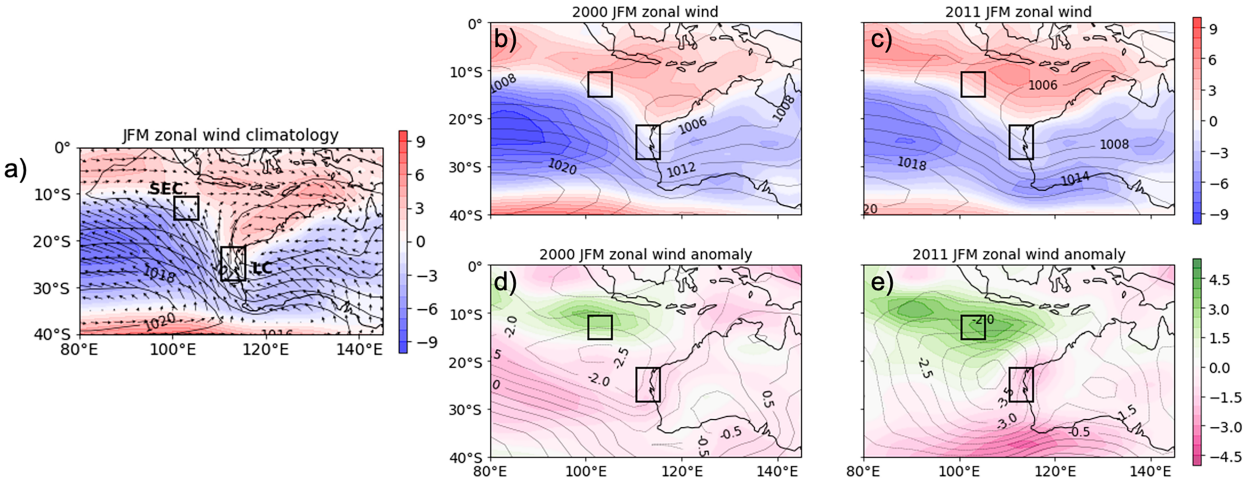

FIG. 13. Zonal wind speed (m s^{-1}) at 1000 hPa (colored shading) and MSLP (hPa; black contour lines): (a) Climatological average of JFM, with reds indicating westerly winds and blues indicating easterly winds. Vectors show wind velocity. Zonal winds and MSLP during JFM of (b) 2000 and (c) 2011, with colored shading as in (a). Also shown for (d) 2000 and (e) 2011 are JFM zonal wind anomaly from the climatology (colored shading, with greens as positive anomalies that are stronger eastward and weaker westward and purples as negative anomalies that are stronger westward and weaker eastward). MSLP anomalies are shown as black contours. A negative MSLP anomaly is present off the western coast of Australia during JFM of both 2000 and 2011. Positive zonal wind anomalies along 10°S are also present, although they are weaker in 2000 than in 2011.

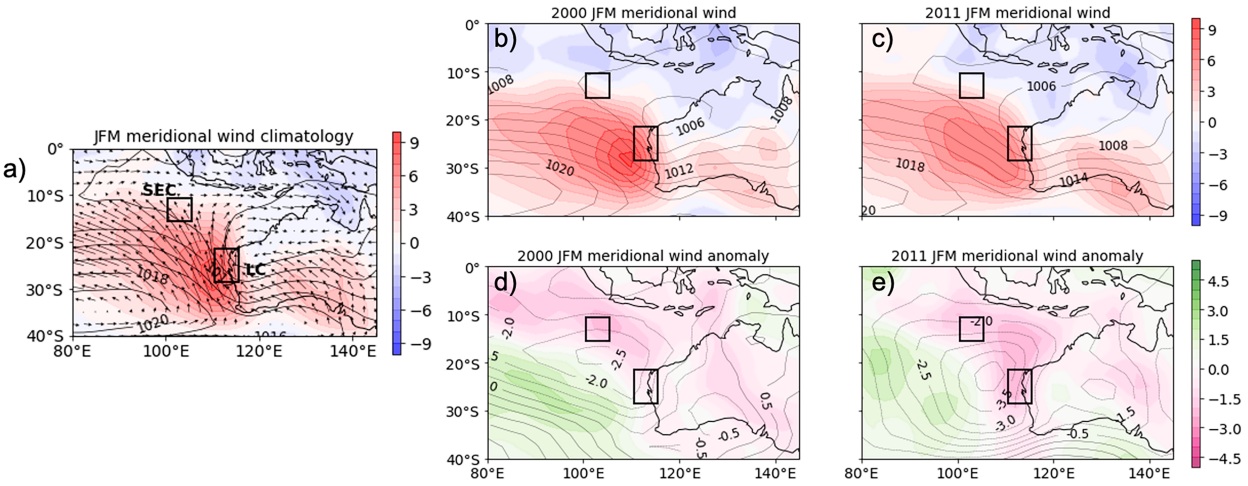

FIG. 14. As in Fig. 6, but for meridional wind speed. In (a), reds indicate southerly winds and blues indicate northerly winds. In (d) and (e), the positive anomalies are stronger northward and weaker southward and the negative anomalies are stronger southward and weaker northward. The low pressure center off the west Australian coast during 2000 and 2011 is associated with anomalous cyclonic atmospheric circulation and a weakening of southerly winds in the LC region. This negative meridional wind anomaly is stronger in 2011 than in 2000.

be due to the presence of La Niña events (2008 and 2011) at the beginning of the time series, which would tend to increase LC flow during austral fall. This was followed by a relatively neutral period and then the large 2015 El Niño, which would decrease the strength of the LC. The progression from La Niña to neutral to El Niño states could present as a trend toward smaller-amplitude seasonal cycles in the LC. Although the SEC is not as well correlated with ENSO as is the LC, the same trend from La Niña to El Niño could play a role. Further analysis of the weakening trend in the SEC is beyond the scope of this paper but is an avenue for future work.

5. Summary

The ITF waters exiting the Indo-Australian are split between the western pathway of the SEC and the southern pathway of the LC. The transport partition of the ITF outflow between these two pathways is not constant but varies in response to larger-scale regional wind forcing. Ningaloo Niño events in particular set up changes in the atmospheric circulation that influence both the SEC and the LC. An anomalous low pressure center off the northwest Australian coast and resulting cyclonic atmospheric circulation are characteristic of these events. During the 2011 and the somewhat weaker 2000 events, oceanic circulation shifted from the SEC as the primary conduit for the ITF water, to a reversal of flow in the SEC region and an anomalous strengthening of the LC. Throughout the Argo observational period of 2005–18, the SEC and LC acted in tandem, with one pathway's export decreasing and the other's increasing. In the context of heat transport the shift between these two pathways is important for local marine ecosystems, especially those off the coast of Australia that experienced changes in habitat and biodiversity during warming events (Wernberg et al. 2012). Climate change will likely alter the ITF, with a potential for a decreased ITF and associated decrease in Pacific to Indian heat transport (0.20 PW less; Ma et al. 2020) in the coming decades. Our study informs this climate change modeling work, showing that an understanding of changes in Indian Ocean heat content will require knowing the ratio of ITF transport entering the SEC to that entering the LC.

Acknowledgments. This work was supported by NASA Headquarters under the NASA Earth and Space Science Fellowship Program, Grant 80NSSC17K0438 "Response of the Indian Ocean to Indonesian Throughflow Variability," and by the Office of Naval Research, Award N00014-22-1-2586.

Data availability statement. The data used in this paper were obtained online (the gridded Argo data used for heat content: http://apdrc.soest.hawaii.edu/projects/argo/; the GODAS reanalysis used for zonal and meridional components of velocity and SSHg: https://www.esrl.noaa.gov/psd/data/gridded/data.godas.html; the Niño-3.4 index: https://www.cpc.ncep.noaa.gov/data/indices/; the DMI: https://www.esrl.noaa.gov/psd/gcos_wgsp/Timeseries/DMI/; the wind speed data: https://www.esrl.noaa.gov/psd/data/gridded/data.ncep.reanalysis.pressure.html).

REFERENCES

Andersson, H. C., and A. Stigebrandt, 2005: Regulation of the Indonesian Throughflow by baroclinic draining of the North Australian Basin. *Deep-Sea Res. I*, **52**, 2214–2233, https://doi.org/10.1016/j.dsr.2005.06.014.

Behringer, D. W., and Y. Xue, 2004: Evaluation of the global ocean data assimilation system at NCEP: The Pacific Ocean.

Eighth Symp. on Integrated Observing and Assimilation Systems for Atmosphere, Oceans, and Land Surface, Seattle, WA, Amer. Meteor. Soc., 2.3, https://ams.confex.com/ams/pdfpapers/70720.pdf.

Benthuysen, J., M. Feng, and L. Zhong, 2014: Spatial patterns of warming off Western Australia during the 2011 Ningaloo Niño: Quantifying impacts of remote and local forcing. *Cont. Shelf Res.*, **91**, 232–246, https://doi.org/10.1016/j.csr.2014.09.014.

Clarke, A. J., and J. Li, 2004: El Niño/La Niña shelf edge flow and Australian western rock lobsters. *Geophys. Res. Lett.*, **31**, L11301, https://doi.org/10.1029/2003GL018900.

Durgadoo, J. V., S. Rühs, A. Biastoch, and C. W. B. Böning, 2017: Indian Ocean sources of Agulhas leakage. *J. Geophys. Res. Oceans*, **122**, 3481–3499, https://doi.org/10.1002/2016JC012676.

Feng, M., G. Meyers, A. Pearce, and S. Wijiffels, 2003: Annual and interannual variations of the Leeuwin Current at 32°S. *J. Geophys. Res.*, **108**, 3355, https://doi.org/10.1029/2002JC001763.

——, M. J. McPhaden, S.-P. Xie, and J. Hafner, 2013: La Niña forces unprecedented Leeuwin Current warming in 2011. *Sci. Rep.*, **3**, 1277, https://doi.org/10.1038/srep01277.

Godfrey, J. S., and T. J. Golding, 1981: The Sverdrup relation in the Indian Ocean, and the effect of Pacific–Indian Ocean throughflow on the Indian Ocean circulation and on the East Australian Current. *J. Phys. Oceanogr.*, **11**, 771–779, https://doi.org/10.1175/1520-0485(1981)011<0771:TSRITI>2.0.CO;2.

——, and K. R. Ridgway, 1985: The large-scale environment of the poleward flowing Leeuwin Current, Western Australia: Longshore steric height gradients, wind stresses and geostrophic flow. *J. Phys. Oceanogr.*, **15**, 481–495, https://doi.org/10.1175/1520-0485(1985)015<0481:TLSEOT>2.0.CO;2.

Gordon, A. L., 1986: Interocean exchange of thermocline water. *J. Geophys. Res.*, **91**, 5037–5046, https://doi.org/10.1029/JC091iC04p05037.

——, S. Ma, D. B. Olson, P. Hacker, A. Ffield, L. D. Talley, D. Wilson, and M. Baringer, 1997: Advection and diffusion of Indonesian Throughflow water within the Indian Ocean south equatorial current. *Geophys. Res. Lett.*, **24**, 2573–2576, https://doi.org/10.1029/97GL01061.

——, and Coauthors, 2010: The Indonesian Throughflow during 2004–2006 as observed by the INSTANT program. *Dyn. Atmos. Oceans*, **50**, 115–128, https://doi.org/10.1016/j.dynatmoce.2009.12.002.

Gruenburg, L. K., and A. L. Gordon, 2018: Variability in Makassar Strait heat flux and its effect on the eastern tropical Indian Ocean. *Oceanography*, **31**, 80–87, https://doi.org/10.5670/oceanog.2018.220.

Hirst, A. C., and J. S. Godfrey, 1993: The role of the Indonesian Throughflow in a global ocean model. *J. Phys. Oceanogr.*, **23**, 1057–1086, https://doi.org/10.1175/1520-0485(1993)023<1057:TROITI>2.0.CO;2.

Kalnay, E., and Coauthors, 1996: The NCEP/NCAR 40-Year Reanalysis Project. *Bull. Amer. Meteor. Soc.*, **77**, 437–472, https://doi.org/10.1175/1520-0477(1996)077<0437:TNYRP>2.0.CO;2.

Kataoka, T., T. Tozuka, S. Behera, and T. Yamagata, 2014: On the Ningaloo Niño/Niña. *Climate Dyn.*, **43**, 1463–1482, https://doi.org/10.1007/s00382-013-1961-z.

——, S. Masson, T. Izumo, T. Tozuka, and T. Yamagata, 2018: Can Ningaloo Niño/Niña develop without El Niño–Southern Oscillation? *Geophys. Res. Lett.*, **45**, 7040–7048, https://doi.org/10.1029/2018GL078188.

Kusunoki, H., S. Kido, and T. Tozuka, 2021: Air-sea interaction in the western tropical Pacific and its impact on asymmetry of the Ningaloo Niño/Niña. *Geophys. Res. Lett.*, **48**, e2021GL093370, https://doi.org/10.1029/2021GL093370.

Lee, S.-K., W. Park, M. O. Baringer, A. L. Gordon, B. Huber, and Y. Liu, 2015: Pacific origin of the abrupt increase in Indian Ocean heat content during the warming hiatus. *Nat. Geosci.*, **8**, 445–449, https://doi.org/10.1038/ngeo2438.

Ma, J., M. Feng, J. Lan, and D. Hu, 2020: Projected future changes in the meridional heat transport and heat balance in the Indian Ocean. *Geophys. Res. Lett.*, **47**, e2019GL086803, https://doi.org/10.1029/2019GL086803.

Marshall, A. G., H. H. Hendon, M. Feng, and A. Schiller, 2015: Initiation and amplitude of the Ningaloo Niño. *Climate Dyn.*, **45**, 2367–2385, https://doi.org/10.1007/s00382-015-2477-5.

Meyers, G., 1996: Variation of Indonesian Throughflow and the El Niño-Southern Oscillation. *J. Geophys. Res.*, **101**, 12 255–12 263, https://doi.org/10.1029/95JC03729.

Nieves, V., J. K. Willis, and W. C. Patzert, 2015: Recent hiatus caused by decadal shift in Indo-Pacific heating. *Science*, **349**, 532–535, https://doi.org/10.1126/science.aaa4521.

Schott, F. A., and J. P. McCreary Jr., 2001: The monsoon circulation of the Indian Ocean. *Prog. Oceanogr.*, **51** (1), 1–123, https://doi.org/10.1016/S0079-6611(01)00083-0.

Smith, R. L., A. Huyer, J. S. Godfrey, and J. A. Church, 1991: The Leeuwin Current off Western Australia, 1986–1987. *J. Phys. Oceanogr.*, **21**, 323–345, https://doi.org/10.1175/1520-0485(1991)021<0323:TLCOWA>2.0.CO;2.

Song, Q., A. L. Gordon, and M. Visbeck, 2004: Spreading of the Indonesian Throughflow in the Indian Ocean. *J. Phys. Oceanogr.*, **34**, 772–792, https://doi.org/10.1175/1520-0485(2004)034<0772:SOTITI>2.0.CO;2.

Thompson, R. O. R. Y., 1984: Observations of the Leeuwin Current off Western Australia. *J. Phys. Oceanogr.*, **14**, 623–628, https://doi.org/10.1175/1520-0485(1984)014<0623:OOTLCO>2.0.CO;2.

Tozuka, T., T. Kataoka, and T. Yamagata, 2014: Locally and remotely forced atmospheric circulation anomalies of Ningaloo Niño/Niña. *Climate Dyn.*, **43**, 2197–2205, https://doi.org/10.1007/s00382-013-2044-x.

van Sebille, E., J. Sprintall, F. U. Schwarzkopf, A. S. Guota, A. Santoso, M. H. England, A. Biastoch, and C. W. Boning, 2014: Pacific-to-Indian Ocean connectivity: Tasman leakage, Indonesian Throughflow, and the role of ENSO. *J. Geophys. Res. Oceans*, **119**, 1365–1382, https://doi.org/10.1002/2013JC009525.

Vidya, P. J., M. Ravichandran, M. P. Subeesh, S. Chatterjee, and M. Nuncio., 2020: Global warming hiatus contributed weakening of the Mascarene High in the southern Indian Ocean. *Sci. Rep.*, **10**, 3255, https://doi.org/10.1038/s41598-020-59964-7.

Waite, A. M., and Coauthors, 2007: The Leeuwin Current and its eddies: An introductory overview. *Deep-Sea Res. II*, **54**, 789–796, https://doi.org/10.1016/j.dsr2.2006.12.008.

Wernberg, T., D. A. Smale, F. Tuya, M. S. Thomsen, T. J. Langlois, T. de Bettignies, S. Bennett, and C. S. Rousseaux, 2012: An extreme climatic event alters marine ecosystem

structure in a global biodiversity hotspot. *Nat. Climate Change*, **3**, 78–82, https://doi.org/10.1038/nclimate1627.

Wyrtki, K., 1961: Physical oceanography of Southeast Asian waters. NAGA Rep. 2, 226 pp., https://escholarship.org/content/qt49n9x3t4/qt49n9x3t4.pdf.

Zhang, L., W. Han, Y. Li, and T. Shinoda, 2018: Mechanisms for generation and development of the Ningaloo Nino. *J. Climate*, **31**, 9239–9259, https://doi.org/10.1175/JCLI-D-18-0175.1.

Zhang, Y., M. Feng, Y. Du, H. E. Phillips, N. L. Bindoff, and M. J. McPhaden, 2018: Strengthened Indonesian Throughflow drives decadal warming in the Southern Indian Ocean. *Geophys. Res. Lett.*, **45**, 6167–6175, https://doi.org/10.1029/2018GL078265.